

Cite this: *J. Mater. Chem. A*, 2018, 6, 20421

# Stitchable supercapacitors with high energy density and high rate capability using metal nanoparticle-assembled cotton threads†

Dongyeeb Shin,<sup>a</sup> Cheong Hoon Kwon,<sup>a</sup> Yongmin Ko,<sup>ab</sup> Byeongyong Lee,<sup>b</sup> Seung Woo Lee<sup>\*b</sup> and Jinhan Cho<sup>\*a</sup>

Herein, we introduce a high-performance and highly flexible asymmetric supercapacitor that is prepared from metallic cotton threads coated with pseudocapacitive nanoparticles without the aid of carbon-based conductive materials. In this study, Au nanoparticles are layer-by-layer assembled on highly porous cotton threads using amine-functionalized molecular linkers in organic media for the preparation of metallic cotton threads that can store a large amount of pseudocapacitive nanoparticles. The highly porous metallic cotton threads exhibit exceptional electrical conductivity ( $\sim 2.1 \times 10^4 \text{ S cm}^{-1}$ , resistance of  $\sim 0.1 \Omega \text{ cm}^{-1}$ ) and yet maintain the intrinsic flexibility of cotton. Using the same assembly method,  $\text{Fe}_3\text{O}_4$  and MnO nanoparticles are deposited onto the metallic cotton threads to prepare the anode and the cathode, respectively, of the asymmetric supercapacitors, and furthermore, Au nanoparticles are periodically inserted between the pseudocapacitive multilayers to facilitate charge transport. The assembled all solid-state asymmetric supercapacitors with a unique structural design deliver a notable areal energy density of  $80.7 \mu\text{W h cm}^{-2}$  (at  $172.5 \mu\text{W cm}^{-2}$ ) and a power density of  $3450.1 \mu\text{W cm}^{-2}$  (at  $53.7 \mu\text{W h cm}^{-2}$ ), exceeding the performance of conventional thread-type asymmetric supercapacitors. We also emphasize that this energy performance can be further enhanced by increasing the number of metal and/or pseudocapacitive nanoparticle layers deposited.

Received 16th July 2018  
Accepted 26th September 2018

DOI: 10.1039/c8ta06840b

rsc.li/materials-a

## 1. Introduction

Wearable electronic devices in connection with Internet of Things (IoT) devices are increasingly penetrating our daily lives. For example, smart garments, which consist of an advanced pattern of functional wearable electronic devices, can potentially be applied in sportswear, medical gowns, and military uniforms.<sup>1–4</sup> For the sustainable development of these wearable electronics, one of the most critical challenges is the preparation of a power source that should have the following three well-balanced features: (1) high electrochemical performance (*e.g.*, a high power density, high energy density, and reliable cycling life), (2) high mechanical flexibility, and (3) versatile fabrication process.<sup>5–10</sup> In this regard, flexible supercapacitors (SCs) have been considered as one of the most promising candidates for powering next-generation wearable electronic devices.<sup>11–17</sup> In particular, one-dimensional SCs (1D-SCs) in the form of fibers or threads have attracted considerable attention because of their

excellent ability to be integrated into wearable electronic devices with arbitrary shapes and flexibility, thereby enabling innovative device design.<sup>18–25</sup> For example, Qin *et al.* reported flexible solid-state 1D-SCs with an energy density of  $6.8 \text{ mW h cm}^{-3}$ , which is much higher than that of other carbon-based 1D-SCs, using nitrogen/oxygen-rich porous carbon fibers.<sup>26</sup>

However, in most cases, carbon (mainly, carbon nanotube (CNT))-based fiber electrodes require spin-based fabrication techniques that use costly and sophisticated processes, and also have substantial difficulty in satisfying the effective long-distance electron transport required in the fiber or yarn format because of their low electrical conductivity below  $300 \text{ S cm}^{-1}$ . Furthermore, continuous weaving or knitting is likely to induce mechanical fracture of the carbon yarns due to the high tensile stress generated from the friction at the contact area between the yarn and the knitting machine parts. To overcome these issues and prepare high-performance 1D-SCs, a variety of electrochemically active carbon materials and pseudocapacitive (PC) materials have been assembled on metal wires (Pt, Au, Ni, stainless-steel, or Cu wires).<sup>27–35</sup> However, the smooth surface of the metal wires limits the loading amount of the PC materials despite their excellent electrical conductivity and mechanical strength. Even though PC materials can be densely coated onto the metal wires through additional treatments, the increased amount of PC materials, which generally

<sup>a</sup>Department of Chemical and Biological Engineering, Korea University, 145 Anam-ro, Seongbuk-gu, Seoul 02841, Republic of Korea. E-mail: jinhan71@korea.ac.kr

<sup>b</sup>The George W. Woodruff School of Mechanical Engineering, Georgia Institute of Technology, Atlanta, Georgia 30332, USA. E-mail: seung.lee@me.gatech.edu

† Electronic supplementary information (ESI) available. See DOI: 10.1039/c8ta06840b

have insulating properties, notably diminishes the contribution of the metal wires to the electrical conductivity, thereby reducing the power density.<sup>28–33</sup> This typical trade-off between the power density and the energy density is more pronounced in 1D-SCs than in two-dimensional (2D)- or three-dimensional (3D)-SCs due to their smaller volume.

As an alternative, electroless metal deposition onto commercial cotton or polyester yarns has been introduced as a method to prepare current collectors for 1D-SCs (in particular, the electrical resistance of electroless Ni-coated cotton yarn is  $\sim 2.2\text{--}1.3\ \Omega\ \text{cm}^{-1}$ ).<sup>25</sup> For example, 1D-SCs with an extremely high power density but relatively low energy density were prepared using electroless Ni deposition on polyester or cotton yarns and subsequent deposition of electrochemically active rGO onto the Ni-coated polyester (areal energy density of  $\sim 1.6\ \mu\text{W h cm}^{-2}$ ; areal power density of  $\sim 2420\ \mu\text{W cm}^{-2}$ )<sup>36</sup> or Ni-coated cotton fibers (volumetric energy density of  $\sim 6.1\ \text{mW h cm}^{-3}$ ; volumetric power density of  $\sim 1400\ \text{mW cm}^{-3}$ ).<sup>25</sup> However, the electroless deposition method needs fine control of metal precursor/reducing agent concentrations and dipping time for depositing a uniform and homogeneous metal (or metal oxide) layer onto the porous 1D-substrates, otherwise the agglomeration of electroless deposition materials can block the porous structure of the substrates with large surface areas. Additionally, various high-energy PC nanomaterials, when compared to CNTs or rGOs, are more difficult to incorporate into the electroless metal-deposited 1D-fibers due to unfavorable mutual interfacial interactions, which limit the preparation of 1D SCs with high energy density.

In view of this, the control of the interfacial structure and composition as well as of the affinity between the fibers (including CNT yarns, metal wires, cotton, and polyester) and the electrochemically active components is essential for further improving the electrochemical performance and long-term stability of 1D-SCs. Many research groups have demonstrated that layer-by-layer (LbL) assembly based on complementary interactions (*i.e.*, electrostatic, hydrogen-bonding, or covalent bonding interactions) between neighboring components provides a simple route to the fabrication of functional multi-layered films with controlled thickness, desired loading amount and tailored chemical composition on substrates of various sizes and shapes.<sup>37–50</sup> In most cases for preparing LbL assembly-based SCs, electrostatically charged CNTs were mainly LbL-assembled with oppositely charged carbon-based materials, conducting polymers, or PC NPs onto 2D supports. Although the LbL approach has not been employed for porous 1D substrates for SC applications, we envision that 1D-SCs can be systematically prepared through the LbL assembly of conductive metal and PC NPs on porous 1D substrates. Furthermore, their performance can be significantly improved through the fine control of the interfacial structures and the loading amount of metal and PC NPs (only by deposition layer number) on the substrates. In particular, if metal NPs (for the preparation of conductive 1D current collectors) and PC NPs (for high energy reservoirs) with diameters below 20 nm are LbL-assembled with small organic linkers instead of bulky polymer linkers (or CNTs) onto microporous 1D substrates, it is anticipated that these

functional NPs will be uniformly coated on the whole region ranging from the interior to the outer surfaces of the substrates maintaining their porous structure.

Herein, we introduce a metallic cotton thread (MCT)-based 1D-asymmetric SC (ASC) with outstanding energy density, high power density, natural cotton-like flexibility, large surface area (due to its porous structure) and excellent operational stability that was prepared using LbL-assembled metal NPs and PC NPs without carbon-based materials or bulky polymer linkers (Fig. 1). In our study, the porous cotton threads composed of numerous cellulose fibrils with hydroxyl (OH) groups have hydrogen-bonding interactions with amine-functionalized organics, and resultantly can store a large amount of conductive metal and PC NPs showing high affinity with amine ( $\text{NH}_2$ ) groups through consecutive LbL assembly. We first convert the insulating cotton threads to MCTs with exceptional conductivity ( $\sim 2.1 \times 10^4\ \text{S cm}^{-1}$ , resistance of  $\sim 0.1\ \Omega\ \text{cm}^{-1}$ ) and cotton-like flexibility. This dramatic conversion is achieved *via* a uniform and dense coating of 8 nm-sized Au NPs on cotton threads through ligand-exchange LbL assembly induced by amine-functionalized molecular linkers. It should be noted that this electrical performance of the MCT outperforms that of electroless deposition- or carbon-based fibers.

On the surface of the formed MCTs, PC NPs such as 7 nm-sized  $\text{Fe}_3\text{O}_4$  and 10 nm-sized MnO NPs were LbL assembled with the same organic molecules using chemically stable covalent bonding interaction to prepare the 1D-anode and 1D-cathode, respectively. The areal energy density of the MCT-based 1D-SCs could be finely controlled by adjusting the number of PC NP layers deposited. We further demonstrate that control of the interfacial structure, that is, the periodic introduction of metal NP layers between the insulating PC NP layers, can significantly improve the electrochemical performance of the 1D-SCs by facilitating electrical communication between the PC NP layers. The assembled MCT-based 1D-ASCs exhibit

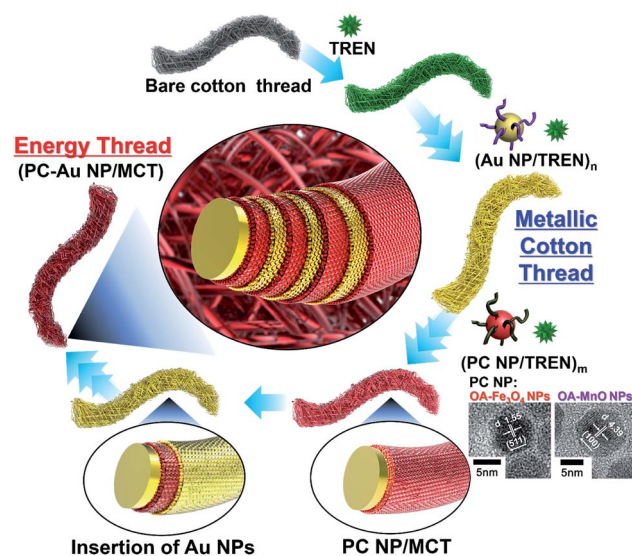


Fig. 1 Schematic illustration of the preparation of the MCT-based 1D-ASCs *via* LbL assembly.

a remarkable energy density (*i.e.*, areal and volumetric energy densities of  $80.7 \mu\text{W h cm}^{-2}$  and  $12.6 \text{ mW h cm}^{-3}$ , respectively), high power density (*i.e.*, areal and volumetric power densities of  $3450.1 \mu\text{W cm}^{-2}$  and  $537.7 \text{ mW cm}^{-3}$ , respectively), and high operational stability, outperforming the previously reported 1D-ASCs. We also highlight that these energy performance indexes can be further enhanced by increasing the number of PC NP layers, and the resultant MCT-based 1D-ASC is stitchable while maintaining the high mechanical flexibility of the natural cotton threads.

## 2. Experimental section

### 2.1. Synthesis of TOABr–Au NPs

Tetraoctylammonium bromide (TOABr)-stabilized Au nanoparticles (NPs) with a diameter of 8 nm were synthesized in toluene using a two-phase reaction.<sup>51</sup> Gold(III) chloride trihydrate (Sigma-Aldrich) in deionized water ( $30 \text{ mmol L}^{-1}$ , 30 mL) and TOABr in toluene ( $20 \text{ mmol L}^{-1}$ , 80 mL) were mixed under vigorous stirring.  $\text{NaBH}_4$  (Sigma-Aldrich) in deionized water ( $0.4 \text{ mol L}^{-1}$ , 25 mL) was added to the above mixture. After 3 h, the mixture was repeatedly washed with  $\text{H}_2\text{SO}_4$  ( $0.1 \text{ mol L}^{-1}$ ),  $\text{NaOH}$  ( $0.1 \text{ mol L}^{-1}$ ), and deionized water. TOABr–Au NPs in toluene were finally obtained after the separation of the aqueous solution.

### 2.2. Synthesis of OA– $\text{Fe}_3\text{O}_4$ NPs

Oleic acid (OA)-stabilized  $\text{Fe}_3\text{O}_4$  NPs with a diameter of 7 nm were obtained in toluene through a thermal reaction.<sup>52</sup>  $\text{Fe}(\text{acac})_3$  (2 mmol, Sigma-Aldrich), 1,2-hexadecanediol (10 mmol, Alfa Aesar), oleylamine (6 mmol), OA (5 mmol), and benzyl ether (20 mL) were mixed and stirred under a nitrogen atmosphere. The mixture was heated to  $200 \text{ }^\circ\text{C}$  for 2 h and then refluxed ( $\sim 300 \text{ }^\circ\text{C}$ ) for 1 h. The black mixture was cooled to room temperature. Ethanol (40 mL) was added to the black solution, and the solid was separated *via* centrifugation. The product was dissolved in hexane containing OA (0.05 mL) and oleylamine (0.05 mL). OA– $\text{Fe}_3\text{O}_4$  NPs (black-brown powder) were obtained through repetitive purification of the product solution using centrifugation (6000 rpm, 10 min).

### 2.3. Synthesis of OA–MnO NPs

OA–MnO NPs with a diameter of 10 nm were obtained in toluene as previously reported.<sup>53</sup> Manganese(II) chloride tetrahydrate (40 mmol, Sigma-Aldrich), sodium oleate (80 mmol, TCI Co., Ltd.), ethanol (30 mL), *n*-hexane (70 mL), and deionized water (40 mL) were stirred at  $70 \text{ }^\circ\text{C}$  for 12 h. Evaporation of the solution produced a Mn oleate powder (pink color). The Mn oleate powder (1.24 g) was mixed with 1-hexadecene (12.8 mL) at  $70 \text{ }^\circ\text{C}$  for 1 h. The solution was then heated to  $280 \text{ }^\circ\text{C}$  at a heating rate of  $1.9 \text{ }^\circ\text{C min}^{-1}$  under a nitrogen atmosphere and maintained at that temperature for 10 min. The resultant solution was cooled to room temperature. OA–MnO NPs were obtained after purifying the solution using centrifugation.

### 2.4. Fabrication of the metallic cotton thread (MCT)

Commercial cotton thread with a diameter of  $230 \mu\text{m}$  was dipped into a solution of tris(2-aminoethyl) amine (TREN) ( $M_w \sim 146$ ) in ethanol ( $1 \text{ mg mL}^{-1}$ ) for 30 min, after which it was washed with pure ethanol to remove the weakly absorbed TREN and dried in air. The TREN-coated cotton thread was immersed in a solution of TOABr–Au NPs in toluene ( $10 \text{ mg mL}^{-1}$ ) for 30 min, after which it was washed with pure toluene and dried in air. These procedures were repeated until the desired electrical conductivity was obtained.

### 2.5. Fabrication of the *m*-PC–Au NP/MCT electrode

The (TREN/pseudocapacitive NP)<sub>5</sub> and (TREN/TOABr–Au NP)<sub>3</sub> multilayers were alternately deposited onto the MCTs using the same LbL assembly method described above until the desired number (*m*) of pseudocapacitive NP layers was deposited.

### 2.6. Materials characterization

The crystallinity of the PC NPs was investigated by high-resolution transmission electron microscopy (HR-TEM, Tecnai20). The adsorption mechanism of the LbL-assembled multilayers was investigated by Fourier transform infrared (FTIR) spectroscopy in specular mode (Cary 600 spectrometer, Agilent Technologies). The growth of the LbL-assembled multilayers was monitored using UV-Vis spectroscopy (Lambda 35, Perkin Elmer) and a quartz crystal microbalance (QCM) (QCM 200, SRS). The mass change after each adsorption step was calculated from the change in the QCM frequency using the Sauerbrey equation.<sup>54</sup> The surface and cross-sectional morphologies of the MCT electrodes were characterized by field emission scanning electron microscopy (FE-SEM) (Hitachi, S-4800). X-ray photoelectron spectroscopy (XPS) was conducted using an X-TOOL (ULVAC-PHI) equipped with an Al K<sub>α</sub> X-ray source (1486.6 eV, 24.1 W, 15 kV).

### 2.7. Assembly of the solid-state MCT-ASC

The gel electrolyte was prepared by mixing  $\text{Na}_2\text{SO}_4$  (1.7 g) with polyvinyl alcohol (PVA) (6 g) and deionized water (60 mL) at  $90 \text{ }^\circ\text{C}$  for 1 h under vigorous stirring until the mixture became clear. The negative and positive electrodes were immersed in the cooled PVA/ $\text{Na}_2\text{SO}_4$  gel for 5 min. Thereafter, the electrodes were placed parallel to each other and dried under ambient conditions until the gel solidified.

### 2.8. Electrochemical measurements

All the electrochemical measurements were performed with an Ivium-n-Stat system (Ivium Technologies). The electrochemical properties of the *m*-PC–Au NP/MCT and *m*-PC NP/MCT electrodes were evaluated in a three-electrode system composed of a Pt wire (counter) and Ag/AgCl (reference) electrode in a 1 M  $\text{Na}_2\text{SO}_4$  electrolyte. EIS was performed over a frequency range from 100 kHz to 0.1 Hz with a potential amplitude of 0.01 V.

### 2.9. Calculation of the electrochemical capacitance

The electrochemical capacitance ( $C$ ) was calculated from the cyclic voltammetry (CV) or galvanostatic charge/discharge (GCD) curves using the following equations:  $C = \int i(V)dV/2\nu\Delta V$  or  $C = I\Delta t/\Delta V$ , where  $i$  is the current during the CV measurement,  $\nu$  is the scan rate of the CV curve,  $\Delta V$  is the operating voltage window,  $I$  is the discharge current during GCD, and  $\Delta t$  is the discharge time during GCD. For the three electrode system, the areal capacitance ( $C_A$ ), volumetric capacitance ( $C_V$ ), length capacitance ( $C_L$ ), and mass capacitance ( $C_M$ ) were calculated according to the equations:  $C_A = C/A$ ,  $C_V = C/V$ ,  $C_L = C/L$ , and  $C_M = C/M$ , where  $A$  is the surface area,  $V$  is the volume,  $L$  is the length, and  $M$  is the mass of the whole electrode (cotton thread + active materials).  $A$  and  $V$  were calculated according to the equations:  $A = \pi D \times L$  and  $V = \pi(D/2)^2 \times L$ , where  $D$  is the diameter of the electrodes. For the two electrode system, the capacitances ( $C_{\text{cell}}$ ) of the asymmetric supercapacitor were calculated according to the equations:  $C_{\text{cell,A}} = C/A_{\text{cell}}$ ,  $C_{\text{cell,V}} = C/V_{\text{cell}}$ ,  $C_{\text{cell,L}} = C/L_{\text{cell}}$ , and  $C_{\text{cell,M}} = C/M_{\text{cell}}$ , where  $A_{\text{cell}}$  is the surface area,  $V_{\text{cell}}$  is the volume,  $L_{\text{cell}}$  is the length, and  $M_{\text{cell}}$  is the mass of the total device without the electrolyte. The coulombic efficiency ( $\eta$ ) was calculated as:  $\eta = q_d/q_c = It_d/It_c$ , where  $q_d$  and  $q_c$  are the total amounts of discharge and charge of the capacitor from GCD,  $I$  is the current density, and  $t_d$  and  $t_c$  are the discharge and charge times. Energy ( $E$ ), power ( $P$ ), and maximum power density ( $P_{\text{max}}$ ) were calculated from the galvanostatic discharge profiles using the following equations:<sup>55</sup>  $E = C\Delta V^2/2$ ,  $P = E \times 3600/\Delta t$ , and  $P_{\text{max}} = V^2/4RB$ , where  $C$  is the capacitance calculated from the galvanostatic discharge profiles and  $R$  is the resistance determined from  $\Delta iR/2i$ .  $\Delta iR$  is the voltage drop between the first two points, and  $i$  is the applied current in the galvanostatic discharge profile.

## 3. Results and discussion

The organic linker tris(2-aminoethyl) amine (TREN) ( $M_w$  of TREN  $\sim 146$ ) in alcohol was LbL assembled with tetraoctylammonium bromide (TOABr)-stabilized Au NPs having a diameter of  $\sim 8$  nm (TOABr-Au NPs) in toluene on commercial cotton threads with a diameter of 230  $\mu\text{m}$  to form MCTs (denoted as (TREN/TOABr-Au NP) $_n$ /cotton) (Fig. S1<sup>†</sup>). When the TOABr-Au NPs were deposited onto the TREN-coated cotton, the bulky and hydrophobic TOABr ligands that were loosely bound to the surface of the Au NPs were easily replaced with TREN due to the higher affinity between the amine ( $-\text{NH}_2$ ) groups of TREN and the surface of the Au NPs than between the ammonium groups of the TOABr ligands and the surface of the Au NPs, thereby inducing direct covalent bonding between the bottom surface of the Au NPs and the  $\text{NH}_2$  groups of TREN. Although the TOABr ligands remained on the top surface of the Au NPs after this step, the subsequent deposition of TREN eliminated these residual TOABr ligands. This adsorption mechanism of the ligand-exchange LbL method was demonstrated using the Fourier transform infrared (FTIR) spectra of the (TREN/TOABr-Au NP) $_n$  multilayer as a function of the bilayer number ( $n$ ) (Fig. 2a and S2<sup>†</sup>). The C-H stretching peaks

(2850 and 2927  $\text{cm}^{-1}$ ) of the bulky TOABr ligands bound to the surface of the Au NPs and the N-H bending peaks (1546 and 1652  $\text{cm}^{-1}$ ) of TREN were observed from the 1 bilayer of TREN/TOABr-Au NP. When TREN was deposited onto the 1 bilayer film on the outermost TOABr-Au NP layer, the intensities of the C-H stretching peaks decreased, while those of the N-H bending peaks increased. Note that the organic layer existing between adjacent Au NP layers in the (TREN/TOABr-Au NP) $_n$  multilayer structure consists of only TREN molecules. This adsorption mechanism of Au NPs based on the ligand exchange reaction with TREN can decrease the distance between Au NPs, allowing the formation of densely packed Au NP arrays on the cotton threads.

Additionally, when the (TREN/TOABr-Au NP) $_{20}$  multilayers were LbL assembled on the cotton threads, the Au NPs were uniformly and homogeneously coated on the whole fibril surface without any aggregation, thereby preserving the highly porous structure of the original cotton threads, as determined by field-emission scanning electron microscopy (FE-SEM) and energy-dispersive X-ray spectroscopy (EDS) mapping (Fig. 2b and S3<sup>†</sup>). The high quality of this coating was also confirmed by the adsorption behavior, the surface morphology, and the X-ray photoelectron spectroscopy (XPS) analysis of the (TREN/TOABr-Au NP) $_{20}$  multilayers deposited onto nonporous substrates (Fig. S4 and S5<sup>†</sup>). With an increase in the bilayer number ( $n$ ) from 0 to 20, the total loading amount per length of the (TREN/TOABr-Au NP) $_n$  multilayers increased up to 0.49  $\text{mg cm}^{-1}$ , exhibiting a linear growth trend (Fig. 2c). In this case, the mass density of the 20-bilayer-coated cotton was calculated to be 2.81  $\text{g cm}^{-3}$  (for comparison, the mass densities of bare cotton and pure Au wire are 1.64  $\text{g cm}^{-3}$  and 19.3  $\text{g cm}^{-3}$ , respectively). Additionally, the mass ratios of the Au NPs embedded between the multilayers were measured to be  $\sim 98$  and  $\sim 91\%$  by thermogravimetric analysis (TGA) and XPS, respectively (Fig. S5 and S6<sup>†</sup>). The difference in the values obtained by TGA and XPS was attributed to the amount of thermally decomposed ash of the organic components (*i.e.*, TREN and TOABr). Consequently, the total loading amount of Au NPs within the (TREN/TOABr-Au NP) $_{20}$  multilayer-coated threads was approximately 0.45  $\text{mg cm}^{-1}$ .

The Au NP multilayers with minimized Au interparticle distances (*i.e.*, only a TREN layer between Au NPs) exhibited a dramatic change in electrical properties with increasing bilayer number (Fig. 2d). As the bilayer number ( $n$ ) increased from 5 to 120, the electrical conductivity of the (TREN/TOABr-Au NP) $_n$  multilayer-coated cotton threads ( $n$ -MCTs) significantly increased from 90 to  $2.1 \times 10^4$   $\text{S cm}^{-1}$ , whereas the length resistance decreased from 25 to 0.12  $\Omega \text{cm}^{-1}$ . Furthermore, the initial electrical conductivity ( $\sim 4.9 \times 10^3$   $\text{S cm}^{-1}$ , length resistance of  $\sim 0.48$   $\Omega \text{cm}^{-1}$ ) of 150 cm-long (TREN/TOABr-Au NP) $_{20}$ -coated cotton threads stitched onto textiles was maintained even after repeated mechanical deformation for 5000 cycles, suggesting that the stitchable thread can be used as a highly stable electrical conductor (Fig. 2e and f). Although  $\text{NH}_2$ -functionalized polymers such as poly(ethylene imine) (PEI,  $M_w \sim 8000$ ) can also be LbL assembled with TOABr-Au NPs onto cotton threads through the same ligand exchange reaction, the

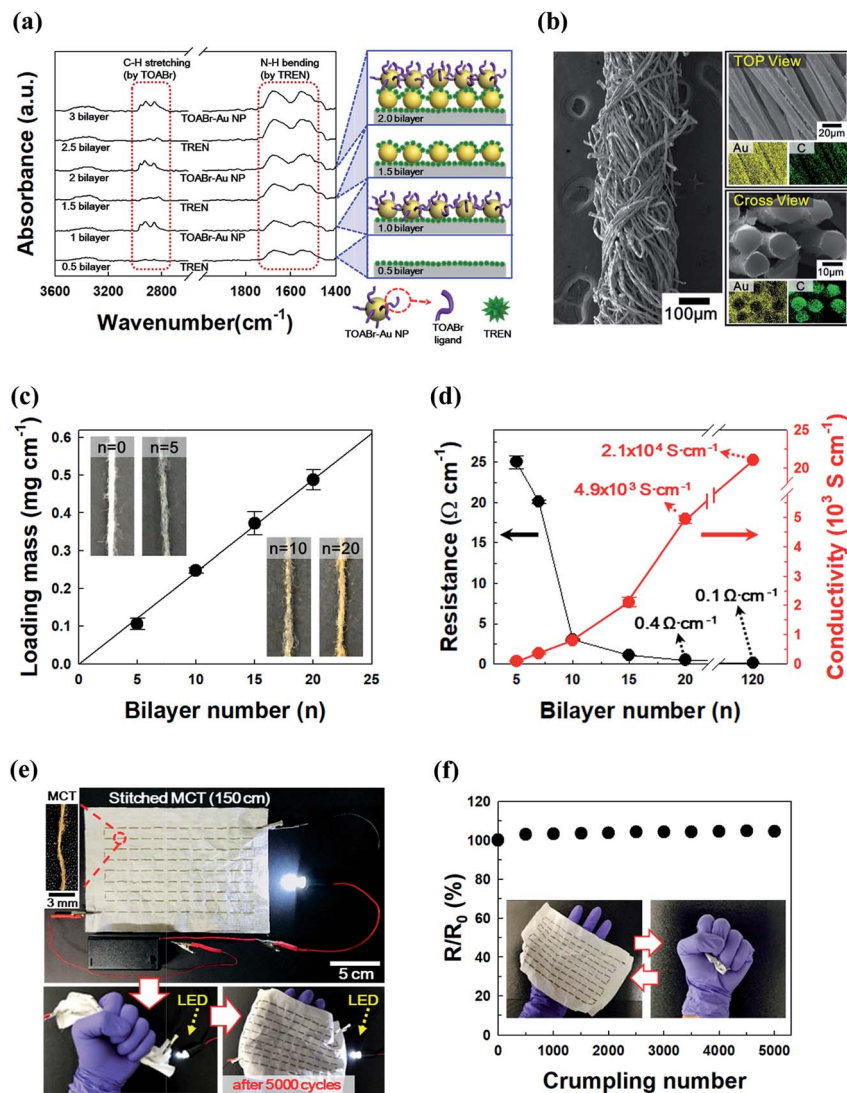


Fig. 2 (a) FTIR spectra of the (TREN/TOABr-Au NP)<sub>n</sub> multilayers as a function of the bilayer number (n). (b) FE-SEM and EDS mapping images of the (TREN/TOABr-Au NP)<sub>20</sub>-coated cotton threads. (c) The loading mass per length of the (TREN/TOABr-Au NP)<sub>n</sub> multilayers on cotton threads as a function of the bilayer number (n). (d) The resistance and electrical conductivity of the (TREN/TOABr-Au NP)<sub>n</sub>-coated cotton threads as a function of the bilayer number (n). (e) Photographs of the stitched (TREN/TOABr-Au NP)<sub>20</sub>-coated cotton threads with a length of 150 cm. LED lit under mechanical deformation. (f) Resistance of the (TREN/TOABr-Au NP)<sub>20</sub>-coated cotton thread under mechanical deformation for 5000 cycles.

interparticle distance between Au NPs significantly increases due to bulky polymer linkers compared to the small TREN linker, resulting in high contact resistance (*i.e.*, low electrical conductivity) (Fig. S7<sup>†</sup>). Furthermore, the charge transfer properties of TREN linker-based electrodes were analyzed using Nyquist plots. As shown in Fig. S8,<sup>†</sup> the internal and charge transfer resistances of (TREN/TOABr-Au NP)<sub>20</sub> were significantly decreased compared to those of (PEI/TOABr-Au NP)<sub>20</sub>. These results clearly imply that both the size of the organic linker and the ligand exchange reaction have a significant effect on the electrical conductivity and charge transfer resistance of the Au NP multilayer-coated cotton threads.

Based on these results, we prepared high-performance 1D-SCs by depositing PC NPs with high energy onto the MCTs which play the role of a conductive framework for the active

materials (hereafter, MCTs are designated as (TREN/TOABr-Au NP)<sub>20</sub>-coated cotton threads). To deposit PC NPs onto MCTs, oleic acid (OA)-stabilized Fe<sub>3</sub>O<sub>4</sub> NPs with a diameter of approximately 7 nm and OA-stabilized MnO NPs with a diameter of approximately 10 nm were prepared and dispersed in toluene, as previously reported<sup>52,53</sup> (Fig. S9<sup>†</sup>). These OA-Fe<sub>3</sub>O<sub>4</sub> and OA-MnO NPs were LbL assembled with TREN on the MCTs through a ligand exchange reaction between the carboxylic group of the OA ligand bound to the surface of the PC NPs and the NH<sub>2</sub> group of TREN to prepare a 1D-anode and 1D-cathode, respectively. The success of these ligand exchange reactions was demonstrated by FTIR analysis (Fig. 3a). When OA-Fe<sub>3</sub>O<sub>4</sub> NPs were deposited on the TREN-coated substrate (*i.e.*, 0.5 bilayer), the OA ligands loosely bound to the surface of the Fe<sub>3</sub>O<sub>4</sub> NPs were replaced with TREN due to the high affinity between the

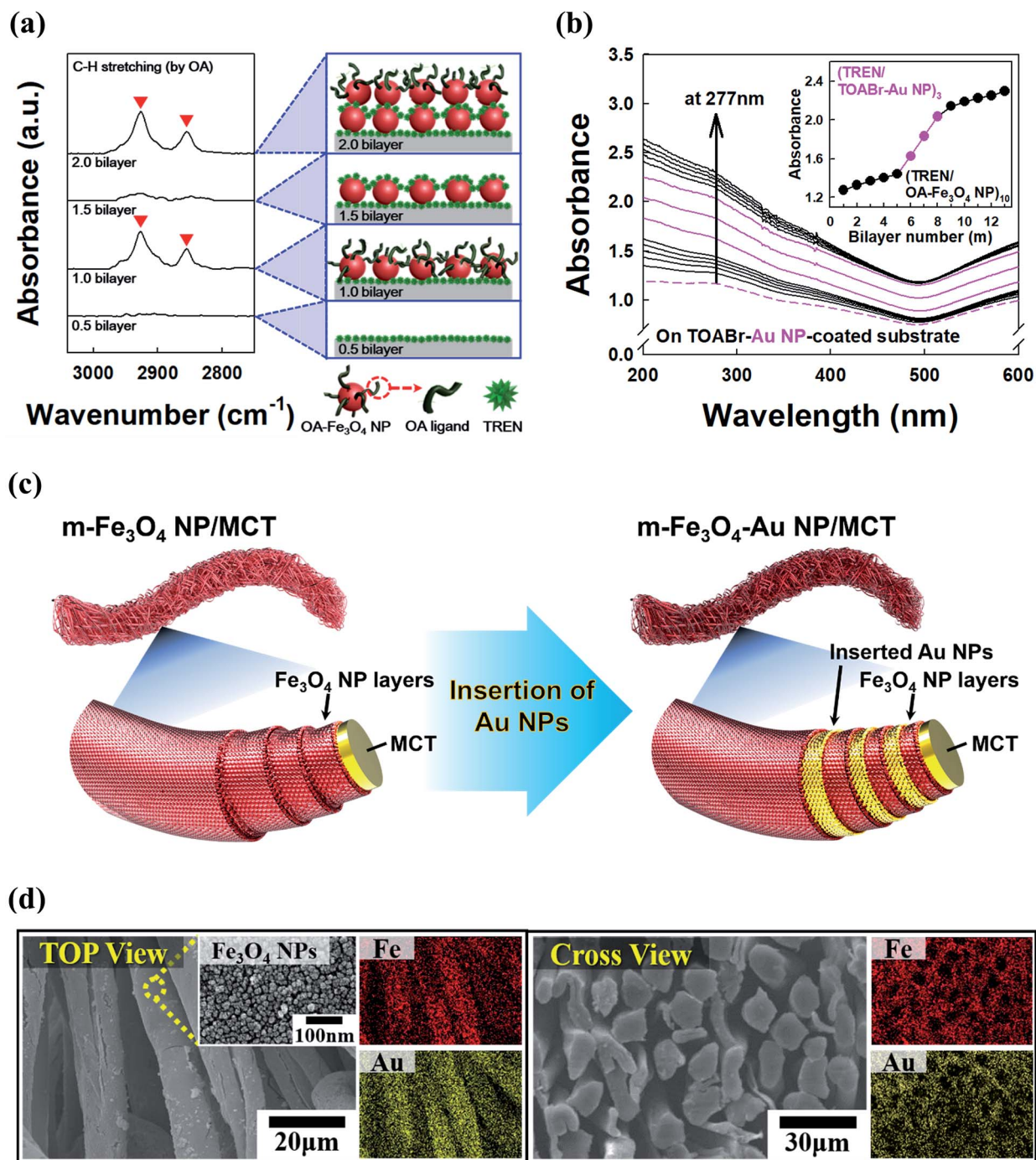


Fig. 3 (a) FTIR spectra of the (TREN/OA-Fe<sub>3</sub>O<sub>4</sub> NP)<sub>m</sub> multilayers as a function of the bilayer number (*m*). (b) UV-Vis spectra of the (TREN/OA-Fe<sub>3</sub>O<sub>4</sub> NP)<sub>5</sub>/(TREN/TOABr-Au NP)<sub>3</sub>/(TREN/OA-Fe<sub>3</sub>O<sub>4</sub> NP)<sub>5</sub> multilayers. (c) Schematic of the *m*-Fe<sub>3</sub>O<sub>4</sub> NP/MCT and *m*-Fe<sub>3</sub>O<sub>4</sub>-Au NP/MCT electrodes. (d) FE-SEM and EDS mapping images of the 40-Fe<sub>3</sub>O<sub>4</sub>-Au NP/MCT electrodes.

amine (-NH<sub>2</sub>) groups of TREN and the surface of the PC NPs (e.g., Fe<sub>3</sub>O<sub>4</sub>, MnO NPs). Additionally, the unremoved OA ligands on the top surface of the Fe<sub>3</sub>O<sub>4</sub> NPs (i.e., 1 bilayer) were eliminated by the subsequent deposition of TREN (i.e., 1.5 bilayer). Therefore, the alternating deposition of TREN and OA-Fe<sub>3</sub>O<sub>4</sub> NPs produces periodic changes in the intensity of the C-H stretching peaks (2853 and 2925 cm<sup>-1</sup>) originating from the long aliphatic chains of the OA ligands bound to the surface of

the Fe<sub>3</sub>O<sub>4</sub> NPs. This assembly mechanism is equally applicable to the OA-MnO NP-based multilayers [i.e., (TREN/OA-MnO NP)<sub>m</sub>] that are employed as the positive electrodes in this study (the details will be discussed later). It should be noted that this ligand-exchange LbL assembly based on a mild and simple dipping process enables stable covalent bonding between metal oxide NPs and the amine-functionalized linker, TREN [i.e., OA-Fe<sub>3</sub>O<sub>4</sub> (or OA-MnO)-NH<sub>2</sub> bonds] (Fig. S10†).

One of the most notable advantages of our approach is that the interfacial structure between the Au NPs and PC NPs can be easily controlled by adjusting the order and number of multilayers (Fig. 3b), and resultantly, the electron transfer properties of the multilayered electrodes can be controlled. To demonstrate this controllability, conductive Au NP layers (*i.e.*, Au NPs after ligand exchange from TOABr to TREN) were periodically inserted between the PC NP layers to promote electron transfer to the neighboring PC NP layers (Fig. 3c). That is, [(TREN/OA-Fe<sub>3</sub>O<sub>4</sub> NP)<sub>5</sub>/(TREN/TOABr-Au NP)<sub>3</sub>]<sub>7</sub>/(TREN/OA-Fe<sub>3</sub>O<sub>4</sub> NP)<sub>5</sub> (*i.e.*, 40-Fe<sub>3</sub>O<sub>4</sub>-Au NP) multilayers composed of 40 Fe<sub>3</sub>O<sub>4</sub> NP layers and 21 Au NP layers were LbL assembled on the MCTs. We confirmed that the 40-Fe<sub>3</sub>O<sub>4</sub>-Au NP multilayers were uniformly deposited on the MCTs, as shown in the EDS maps (Fig. 3d). Additionally, (TREN/OA-Fe<sub>3</sub>O<sub>4</sub> NP)<sub>40</sub> multilayers without Au NPs (40-Fe<sub>3</sub>O<sub>4</sub> NP) were also deposited on the MCTs for the comparison of their electron transfer properties with those of 40-Fe<sub>3</sub>O<sub>4</sub>-Au NP/MCT. The loading amount of the 40-Fe<sub>3</sub>O<sub>4</sub> NPs per length of the MCT was measured to be approximately

0.31 mg cm<sup>-1</sup> by TGA (Fig. S11†). These two different multilayered structures provide a good model system for understanding the role of the Au NPs inserted between the PC NP layers in the observed electrochemical performance.

The electrochemical properties of Fe<sub>3</sub>O<sub>4</sub> NP multilayer-coated MCTs with a fixed length of 1.5 cm were evaluated with a three-electrode system in the potential range of -0.9 to 0.1 V (*vs.* Ag/AgCl) at a scan rate of 5 mV s<sup>-1</sup> in 1 M Na<sub>2</sub>SO<sub>4</sub> electrolyte. The current originating from the double layer capacitance of the Au NPs within the MCTs was found to be negligible. The cyclic voltammetry (CV) scan of the 40-Fe<sub>3</sub>O<sub>4</sub>-Au NP/MCT electrode with periodically inserted Au NP layers exhibited a higher current level with more evident redox peaks than that of the 40-Fe<sub>3</sub>O<sub>4</sub> NP/MCT electrode (Fig. 4a). The redox peaks in a neutral electrolyte such as Na<sub>2</sub>SO<sub>4</sub> can be attributed to the reversible valence change of Fe in the extended potential window of -0.9 to 0.1 V (Fig. S12†).<sup>56,57</sup> Considering the fact that the double layer capacitance of Au NPs is much smaller than the pseudocapacitance of Fe<sub>3</sub>O<sub>4</sub> NPs, the notable increase in the

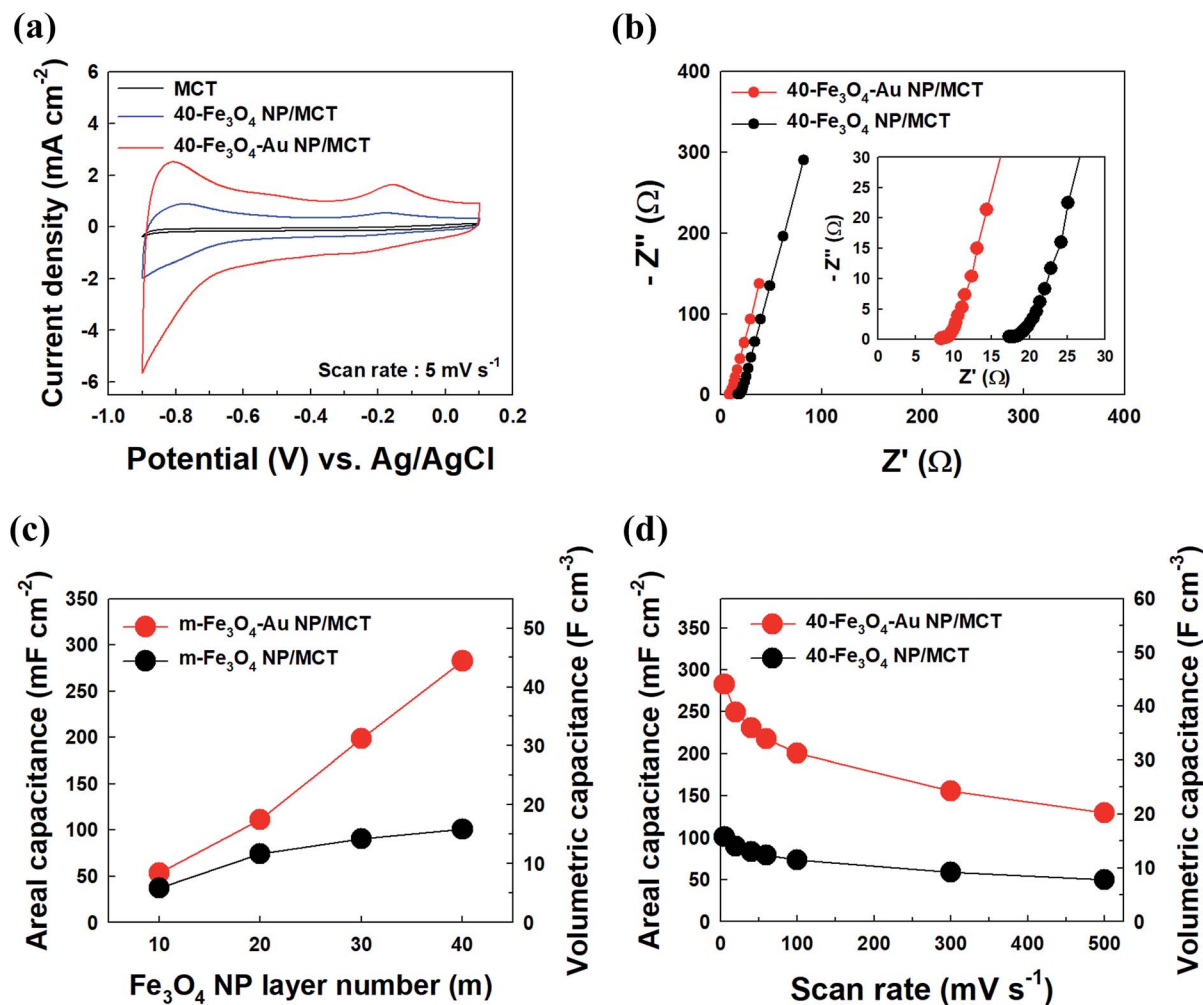


Fig. 4 (a) CV scans of the MCT, 40-Fe<sub>3</sub>O<sub>4</sub> NP/MCT, and 40-Fe<sub>3</sub>O<sub>4</sub>-Au NP/MCT electrodes at a scan rate of 5 mV s<sup>-1</sup>. (b) Nyquist plots of the 40-Fe<sub>3</sub>O<sub>4</sub> NP/MCT and 40-Fe<sub>3</sub>O<sub>4</sub>-Au NP/MCT electrodes. (c) Areal and volumetric capacitances of the *m*-Fe<sub>3</sub>O<sub>4</sub> NP/MCT and *m*-Fe<sub>3</sub>O<sub>4</sub>-Au NP/MCT electrodes as a function of the total Fe<sub>3</sub>O<sub>4</sub> NP layer number (*m*) at a scan rate of 5 mV s<sup>-1</sup>. (d) Areal and volumetric capacitance of the 40-Fe<sub>3</sub>O<sub>4</sub> NP/MCT and 40-Fe<sub>3</sub>O<sub>4</sub>-Au NP/MCT electrodes with increasing scan rate from 5 to 500 mV s<sup>-1</sup>.

electrochemical response of the 40-Fe<sub>3</sub>O<sub>4</sub>-Au NP/MCT electrode suggests that the periodically inserted Au NP layers between the TREN/OA-Fe<sub>3</sub>O<sub>4</sub> NP multilayers facilitate effective pseudocapacitive charge storage in the Fe<sub>3</sub>O<sub>4</sub> layers by providing favorable electron transfer paths. To better clarify this possibility, the internal resistances of the 40-Fe<sub>3</sub>O<sub>4</sub> NP/MCT and 40-Fe<sub>3</sub>O<sub>4</sub>-Au NP/MCT electrodes were investigated by electrochemical impedance spectroscopy (EIS). As shown in Fig. 4b, the equivalent series resistance (ESR) values of the 40-Fe<sub>3</sub>O<sub>4</sub> NP/MCT and 40-Fe<sub>3</sub>O<sub>4</sub>-Au NP/MCT electrodes were approximately 17.3 and 8.3 Ω, respectively. These results strongly imply that the periodically deposited Au NPs can facilitate electron transfer between the electrodes despite the high mass loading of PC NPs with poor conductivity.

Based on the CV results, we quantitatively evaluated the areal and volumetric capacitances of the 40-Fe<sub>3</sub>O<sub>4</sub> NP/MCT and 40-Fe<sub>3</sub>O<sub>4</sub>-Au NP/MCT electrodes (for the anode) (Fig. 4c). Although the areal and volumetric capacitances of the two different electrodes increased with the increasing number of OA-Fe<sub>3</sub>O<sub>4</sub> NP layers, the *m*-Fe<sub>3</sub>O<sub>4</sub>-Au NP/MCT electrode exhibited more significant increases in the areal and volumetric capacitances than the *m*-Fe<sub>3</sub>O<sub>4</sub> NP/MCT electrode without Au NPs. In particular, the areal, volumetric, length and mass capacitances of the 40-Fe<sub>3</sub>O<sub>4</sub>-Au NP/MCT electrode at a scan rate of 5 mV s<sup>-1</sup> were approximately 282.5 mF cm<sup>-2</sup>, 44 F cm<sup>-3</sup>, 22.6 mF cm<sup>-1</sup>, and 12.1 F g<sup>-1</sup> respectively; thus, this electrode outperformed the 40-Fe<sub>3</sub>O<sub>4</sub> NP/MCT electrode (areal capacitance of 100.9 mF cm<sup>-2</sup>, volumetric capacitance of 15.7 F cm<sup>-3</sup>, length capacitance of 8.1 mF cm<sup>-1</sup>, and mass capacitance of 5.7 F g<sup>-1</sup> at the same scan rate). The capacitance from CV was divided by the surface area, volume, length, and mass of the whole electrode (cotton thread + active materials). Another notable feature of this approach is that the capacitance of the MCT-based electrodes can be further increased and precisely controlled by adjusting the layer number of PC NPs, as evidenced by the observation of a linear relationship between the capacitance and layer number (*m*) of Fe<sub>3</sub>O<sub>4</sub> NPs (Fig. S13†). We also highlight that the loading amount of Fe<sub>3</sub>O<sub>4</sub> NPs (or Fe<sub>3</sub>O<sub>4</sub>-Au NPs) deposited on the inner and outer surfaces of the highly porous MCTs linearly increases with the layer number (*m*) of Fe<sub>3</sub>O<sub>4</sub> NPs without a meaningful increase in the total electrode volume (Fig. S14†). Thus, the volumetric capacitance normalized by the total volume of the *m*-Fe<sub>3</sub>O<sub>4</sub>-Au NP/MCT electrode also increased linearly with the increasing layer number (*m*) of the Fe<sub>3</sub>O<sub>4</sub> NPs (Fig. 4c). Furthermore, the 40-Fe<sub>3</sub>O<sub>4</sub>-Au NP/MCT electrode maintained typical PC behavior up to a relatively high scan rate of 500 mV s<sup>-1</sup>, implying its excellent rate capability (Fig. S15†). Although the areal and volumetric capacitance values gradually decreased with the increasing scan rate, the capacitance values of the 40-Fe<sub>3</sub>O<sub>4</sub>-Au NP/MCT electrode were far superior to those of the 40-Fe<sub>3</sub>O<sub>4</sub> NP/MCT electrode due to its enhanced electrical conductivity (Fig. 4d). Using the same ligand-exchange LbL method, we also prepared *m*-MnO NP/MCT and *m*-MnO-Au NP/MCT cathodes with a length of 1.5 cm. The MnO NP-based electrodes exhibited rectangular PC behavior in the potential range of 0 to 0.9 V (*vs.* Ag/AgCl) (Fig. S16†). In the case of the 40-MnO-Au NP/MCT electrode, the ESR and areal, volumetric, length, and mass capacitance

values were approximately 5.9 Ω, 295.8 mF cm<sup>-2</sup>, 46 F cm<sup>-3</sup>, 23.6 mF cm<sup>-1</sup>, and 13 F g<sup>-1</sup>, respectively, at 5 mV s<sup>-1</sup>.

Based on these results, we prepared a 1D-ASC incorporated with Au NPs composed of a 40-Fe<sub>3</sub>O<sub>4</sub>-Au NP/MCT anode and 40-MnO-Au NP/MCT cathode (*i.e.*, 40-Fe<sub>3</sub>O<sub>4</sub>-Au NP/MCT//40-MnO-Au NP/MCT) based on their characteristic potential regions (Fig. 5a and S17†). In this case, poly(vinyl alcohol) (PVA) containing 0.2 M Na<sub>2</sub>SO<sub>4</sub> was used as a solid electrolyte for the 1D-ASCs with a length of 1.5 cm. The potential-dependent CV scan of the 1D-ASCs incorporated with Au NPs measured at a scan rate of 20 mV s<sup>-1</sup> displayed a quasi-rectangular shape up to 1.8 V (Fig. 5b). This stable charge storage behavior was also confirmed by the galvanostatic charge/discharge (GCD) curves (Fig. S18†). In addition, the quasi-rectangular CV and quasi-symmetric triangular GCD curves of the 1D-ASC incorporated with Au NPs obtained at high sweep rates (*i.e.*, a scan rate of 200 mV s<sup>-1</sup> and a high current density of 6.0 mA cm<sup>-2</sup>) reveal the excellent rate capability of the 1D-ASC (Fig. 5c and d). Specifically, the areal capacitance and coulombic efficiency of the 1D-ASC incorporated with Au NPs were calculated from the GCD profiles (Fig. 5e and S19†). The areal capacitance decreased from 179.2 mF cm<sup>-2</sup> (volumetric capacitance of ~27.9 F cm<sup>-3</sup>, length capacitance of 28.6 mF cm<sup>-1</sup>, and mass capacitance of 7.8 F g<sup>-1</sup>) to 119.3 mF cm<sup>-2</sup> (18.6 F cm<sup>-3</sup>, 19.1 mF cm<sup>-1</sup>, and 5.2 F g<sup>-1</sup>) with an increase in the current density from 0.3 to 6.0 mA cm<sup>-2</sup>. Additionally, the 1D-ASC incorporated with Au NPs showed a low coulombic efficiency of 66% at a low current density of 0.3 mA cm<sup>-2</sup> presumably due to the irreversible faradaic reactions leading to current leakages in the low current density region (Fig. S19†).<sup>58,59</sup> However, the coulombic efficiency quickly increased up to ~96% with an increase in the current density (Fig. S19†).

Note that the EIS measurements of the 1D-ASC incorporated with Au NPs exhibited a relatively low ESR value (37.5 Ω) compared to that of the 1D-ASC without Au NPs (*i.e.*, 40-Fe<sub>3</sub>O<sub>4</sub> NP/MCT//40-MnO NP/MCT) (48.9 Ω) (Fig. S20†). These results clearly show that the periodic insertion of Au NP layers between the PC NP multilayers notably enhanced electron transport within the 1D-ASC electrode, resulting in a low total internal resistance for the devices. Additionally, the 1D-ASC incorporated with Au NPs retained 92.3% of its initial capacitance after 5000 cycles (based on GCD measurements) (Fig. 5f), confirming the operational stability of the MCT-based 1D-ASC.

The energy and power densities of MCT-based 1D-ASCs (*i.e.*, 40-Fe<sub>3</sub>O<sub>4</sub>-Au NP/MCT//40-MnO-Au NP/MCT) with a length of 1.5 cm were evaluated using galvanostatic discharge profiles. The Ragone plot shows the calculated areal energy density ( $E_A$ ) and power density ( $P_A$ ) of the 1D-ASCs incorporated with Au NPs at the given current density along with the corresponding values for solid-state fiber (or thread)-type ASCs reported by other research groups (Fig. 5g).<sup>30,32,34,36,60-63</sup> The highest  $E_A$  and  $P_A$  values of the MCT-based 1D-ASCs were 80.7 μW h cm<sup>-2</sup> at 172.5 μW cm<sup>-2</sup> and 3450.1 μW cm<sup>-2</sup> at 53.7 μW h cm<sup>-2</sup>, respectively. Furthermore, the maximum power density was 41.4 mW cm<sup>-2</sup> at 6.0 mA cm<sup>-2</sup>, as calculated from the resistance of the MCT-based 1D-ASCs (see the method);<sup>55</sup> thus, the MCT-based 1D-ASCs outperformed the previously reported 1D-ASCs

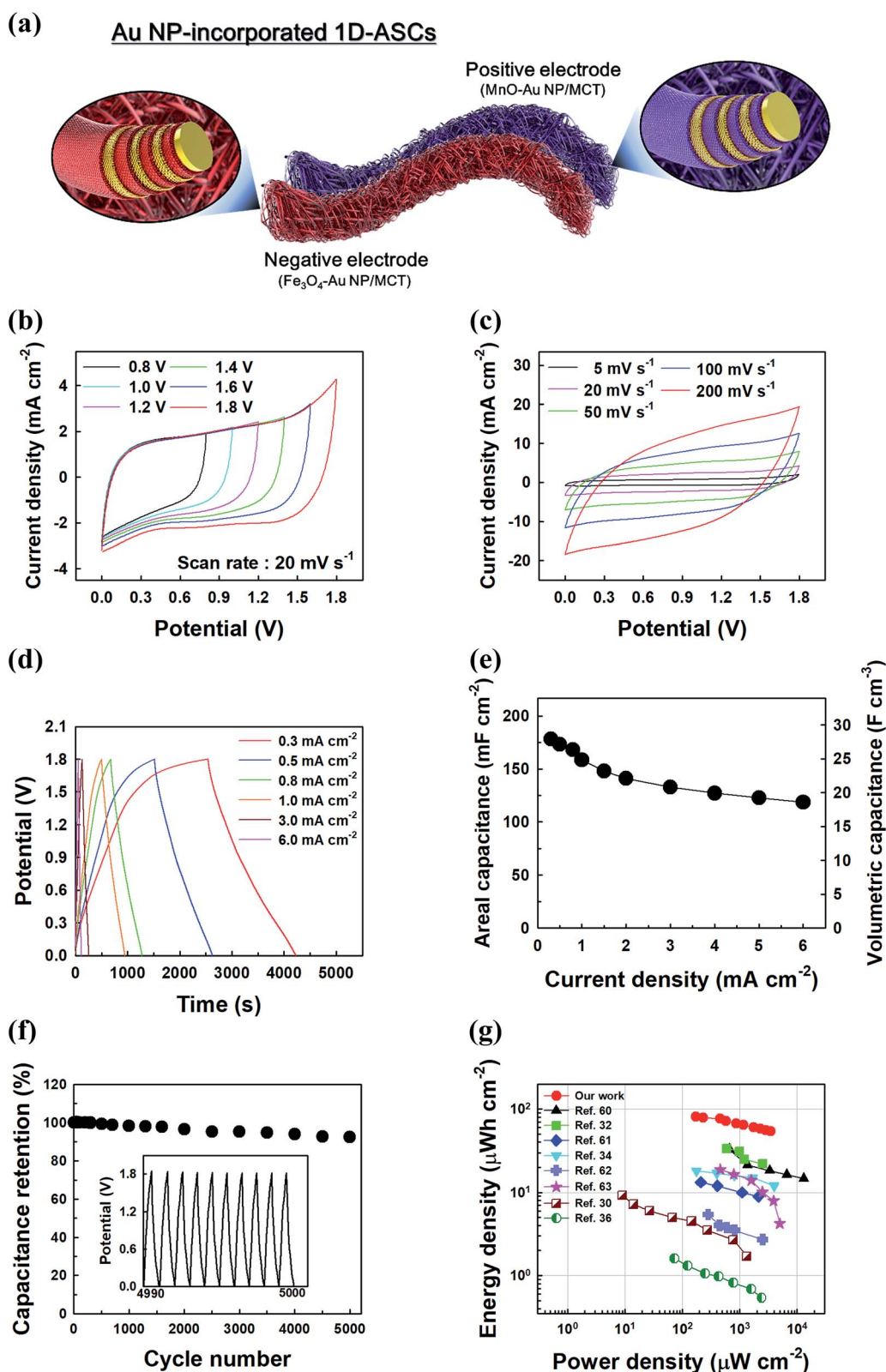


Fig. 5 (a) Schematic of the 1D-ASCs incorporated with Au NPs. (b) CV scans of the 1D-ASCs incorporated with Au NPs tested over different voltages from 0.8 to 1.8 V at a scan rate of 20 mV s<sup>-1</sup>. (c) CV scans of the 1D-ASCs incorporated with Au NPs with the increasing scan rate from 5 to 200 mV s<sup>-1</sup>. (d) GCD curves of the 1D-ASCs incorporated with Au NPs at different current densities from 0.3 to 6.0 mA cm<sup>-2</sup>. (e) Areal and volumetric capacitances of the 1D-ASCs incorporated with Au NPs at different current densities. (f) Cycling stability of the 1D-ASCs incorporated with Au NPs at a current density of 6.0 mA cm<sup>-2</sup>. (g) Ragone-plots of the areal energy and power density of the 1D-ASCs incorporated with Au NPs compared with those of the solid-state fiber (or thread)-type SCs reported by other research groups.

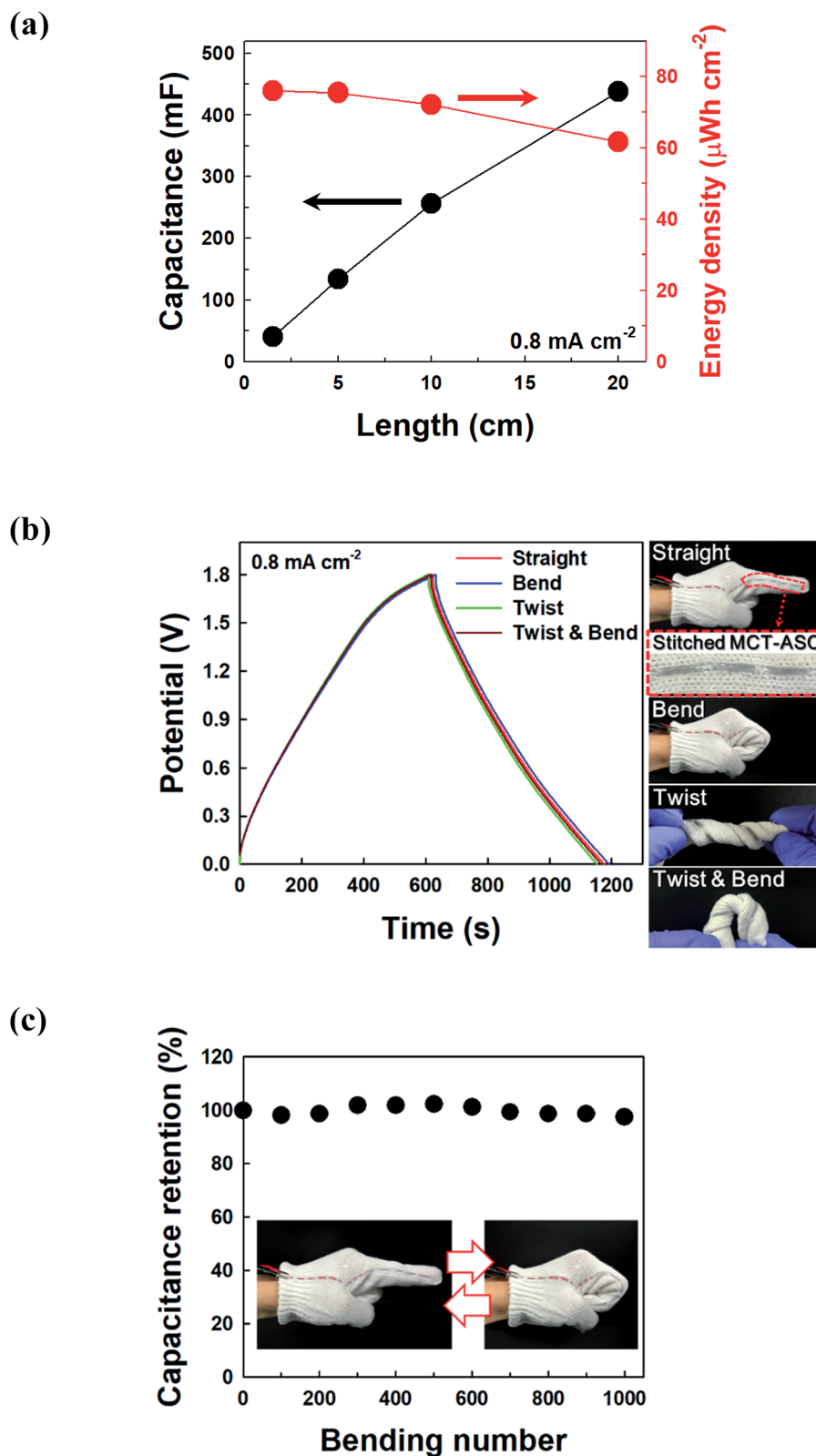


Fig. 6 (a) Capacitance and areal energy density of the 1D-ASCs incorporated with Au NPs at a current density of  $0.8 \text{ mA cm}^{-2}$  as a function of their length. (b) GCD curves of the 1D-ASCs incorporated with Au NPs stitched onto a fabric glove under various deformation conditions. (c) Capacitance retention of the 1D-ASCs incorporated with Au NPs versus the bending number.

(especially in terms of the areal energy density) (Table S1†). Additionally, the volumetric energy density ( $E_V$ ) of the device changed from 8.4 to 12.6 mW h cm<sup>-3</sup> (the length energy density,  $E_L$ , changed from 8.6 to 12.9 μW h cm<sup>-1</sup>; the mass energy density changed from 2.2 to 3.4 W h kg<sup>-1</sup>) in the volumetric power density ( $P_V$ ) range of 537.7–26.9 mW cm<sup>-3</sup> (corresponding to a length power density,  $P_L$ , of 552.1–27.6 μW cm<sup>-1</sup> and a mass power density of 144.1–7.2 W kg<sup>-1</sup>) (Fig. S21†). As mentioned earlier, this energy storage performance could be further improved by increasing the bilayer number.

We also investigated the total capacitance and  $E_A$  as a function of the length of the 1D-ASCs incorporated with Au NPs at a fixed current density of 0.8 mA cm<sup>-2</sup> (Fig. 6a). With an increase in the length from 1.5 to 20 cm, the total capacitance increased from 40.5 to 437.3 mF. Significantly, the high energy density of 76 μW h cm<sup>-2</sup> at 1.5 cm was maintained at 72.1 μW h cm<sup>-2</sup> at 10 cm, and a high energy density of 61.5 μW h cm<sup>-2</sup> was still exhibited even at 20 cm. In addition to the length performance of the thread-type 1D-ASCs, the capability to withstand mechanical deformation is considered as another important factor of the performance. As shown in Fig. 6b, MCT-based 1D-ASCs were first stitched to fabric gloves, and their electrochemical properties were investigated under various mechanical deformation conditions using GCD measurement. The typical triangular-shaped GCD profiles of the 1D-ASCs at 0.8 mA cm<sup>-2</sup> remained almost unchanged under a variety of external deformation conditions, including bending and/or twisting. We also observed that 97.5% of the initial capacitance value was maintained after bending tests for 1000 cycles (Fig. 6c). Based on these results, the MCT-based 1D-ASCs exhibited remarkable energy storage performance with good operational stability while maintaining stitchable flexibility.

## 4. Conclusions

We have demonstrated the fabrication of a high-performance stitchable 1D-ASC with remarkable energy/power density, fast rate capability, and good operational stability by using highly flexible, porous, and conductive MCTs coated with PC NP multilayers. In particular, the ligand-exchange LbL assembly of TOABr–Au NPs and TREN linkers vertically bridged all the interfaces between the Au and PC NPs, and between the cotton threads and Au NPs without the use of inactive polymer binders or linkers. This approach facilitated charge transport between neighboring NPs and furthermore provided systematic control of the interfacial structure and loading amount of Au and PC NPs. Therefore, the MCTs used in our system could serve as an excellent energy reservoir for integrating PC NPs and as a 1D substrate with metal-like conductivity. The periodic deposition of Au NPs into the PC NP multilayers with poor conductivity further enhanced the energy storage performance over that of the PC multilayers without Au NPs. The assembled 1D-ASCs with a structural design of (40-Fe<sub>3</sub>O<sub>4</sub>-Au NP/MCT)/(40-MnO NP-Au NP/MCT) exhibited a notable areal energy density of 80.7 μW h cm<sup>-2</sup> (at 0.3 mA cm<sup>-2</sup>), exceeding those of the conventional thread-type ASCs reported to date. We revealed that this performance could be further enhanced by increasing

the layer number (*i.e.*, loading amount) of Au NPs and/or PC NPs. Considering the fact that low energy density is one of the most critical issues in the field of 1D-ASCs, our approach of using LbL-assembled MCTs can provide a basis for developing and designing high-performance 1D-ASCs and furthermore be widely applied in various electrochemical applications requiring flexibility.

## Conflicts of interest

There are no conflicts to declare.

## Acknowledgements

This work was supported by a National Research Foundation (NRF) grant funded by the Ministry of Science, ICT & Future Planning (MSIP) (2018R1A2A1A05019452; NRF-2016M3A7B4910619).

## Notes and references

- 1 K. Jost, C. R. Perez, J. K. McDonough, V. Presser, M. Heon, G. Dion and Y. Gogotsi, *Energy Environ. Sci.*, 2011, **4**, 5060–5067.
- 2 Y. Shao, M. F. El-Kady, L. J. Wang, Q. Zhang, Y. Li, H. Wang, M. F. Mousavi and R. B. Kaner, *Chem. Soc. Rev.*, 2015, **44**, 3639–3665.
- 3 W. Zeng, L. Shu, Q. Li, S. Chen, F. Wang and X.-M. Tao, *Adv. Mater.*, 2014, **26**, 5310–5336.
- 4 Y. Huang, M. Zhu, Y. Huang, Z. Pei, H. Li, Z. Wang, Q. Xue and C. Zhi, *Adv. Mater.*, 2016, **28**, 8344–8364.
- 5 Q. Huang, D. Wang and Z. Zheng, *Adv. Energy Mater.*, 2016, **6**, 1600783.
- 6 X. Wang, X. Lu, B. Liu, D. Chen, Y. Tong and G. Shen, *Adv. Mater.*, 2014, **26**, 4763–4782.
- 7 M. F. El-Kady and R. B. Kaner, *Nat. Commun.*, 2013, **4**, 1475.
- 8 X. Wang, F. Wan, L. Zhang, Z. Zhao, Z. Niu and J. Chen, *Adv. Funct. Mater.*, 2018, **28**, 1707247.
- 9 Y. Wang, C. Chen, H. Xie, T. Gao, Y. Yao, G. Pastel, X. Han, Y. Li, J. Zhao, K. Fu and L. Hu, *Adv. Funct. Mater.*, 2017, **27**, 1703140.
- 10 H. Pan, J. Chen, R. Cao, V. Murugesan, N. N. Rajput, K. S. Han, K. Persson, L. Estevez, M. H. Engelhard, J.-G. Zhang, K. T. Mueller, Y. Cui, Y. Shao and J. Liu, *Nat. Energy*, 2017, **2**, 813.
- 11 X. Lu, M. Yu, G. Wang, Y. Tong and Y. Li, *Energy Environ. Sci.*, 2014, **7**, 2160–2181.
- 12 K. Jost, G. Dion and Y. Gogotsi, *J. Mater. Chem. A*, 2014, **2**, 10776–10787.
- 13 N. Choudhary, C. Li, J. Moore, N. Nagaiah, L. Zhai, Y. Jung and J. Thomas, *Adv. Energy Mater.*, 2017, **29**, 1605336.
- 14 Z. Wang, P. Tammela, M. Strømme and L. Nyholm, *Adv. Energy Mater.*, 2017, **7**, 1700130.
- 15 Q. Xue, J. Sun, Y. Huang, M. Zhu, Z. Pei, H. Li, Y. Wang, N. Li, H. Zhang and C. Zhi, *Small*, 2017, **13**, 1701827.
- 16 Z. Gao, C. Bumgardner, N. Song, Y. Zhang, J. Li and X. Li, *Nat. Commun.*, 2016, **7**, 11586.

- 17 B. C. Kim, J.-Y. Hong, G. G. Wallace and H. S. Park, *Adv. Energy Mater.*, 2015, **5**, 1500959.
- 18 S. J. Varma, K. S. Kumar, S. Seal, S. Rajaraman and J. Thomas, *Adv. Sci.*, 2018, 1800340.
- 19 Y.-J. Heo, J. W. Lee, Y.-R. Son, J.-H. Lee, C. S. Yeo, T. D. Lam, S. Y. Park, S.-J. Park, L. H. Sinh and M. K. Shin, *Adv. Energy Mater.*, 2018, 1801854.
- 20 M. Zou, W. Zhao, H. Wu, H. Zhang, W. Xu, L. Yang, S. Wu, Y. Wang, Y. Chen, L. Xu and A. Cao, *Adv. Mater.*, 2018, **30**, 1704419.
- 21 C. Choi, J. W. Park, K. J. Kim, K. W. Lee, M. J. Andrade, S. H. Kim, S. Gambhir, G. M. Spinks, R. H. Baughman and S. J. Kim, *RSC Adv.*, 2018, **8**, 13112–13120.
- 22 S. T. Senthilkumar, Y. Wang and H. Huang, *J. Mater. Chem. A*, 2015, **3**, 20863–20879.
- 23 Y.-J. Heo, J. W. Lee, Y.-R. Son, J.-H. Lee, C. S. Yeo, Y. D. Lam, S. Y. Park, S.-J. Park, L. H. Sinh and M. K. Shin, *Adv. Energy Mater.*, 2018, 1801854.
- 24 C. Choi, K. M. Kim, K. J. Kim, X. Lepró, G. M. Spinks, R. H. Baughman and S. J. Kim, *Nat. Commun.*, 2016, **7**, 13811.
- 25 L. Liu, Y. Yu, C. Yan, K. Li and Z. Zheng, *Nat. Commun.*, 2015, **6**, 7260.
- 26 T. Qin, S. Peng, J. Hao, Y. Wen, Z. Wang, X. Wang, D. He, J. Zhang, J. Hou and G. Cao, *Adv. Energy Mater.*, 2017, **7**, 1700409.
- 27 D. Zhang, M. Miao, H. Niu and Z. Wei, *ACS Nano*, 2014, **8**, 4571–4579.
- 28 X. Niu, G. Zhu, Z. Yin, Z. Dai, X. Hou, J. Shao, W. Huang, Y. Zhang and X. Dong, *J. Mater. Chem. A*, 2017, **5**, 22939–22944.
- 29 Y. Huang, M. Zhu, Z. Pei, Q. Xue, Y. Huang and C. Zhi, *J. Mater. Chem. A*, 2016, **4**, 1290–1297.
- 30 Y. Huang, H. Hu, Y. Huang, M. Zhu, W. Meng, C. Liu, Z. Pei, C. Hao, Z. Wang and C. Zhi, *ACS Nano*, 2015, **9**, 4766–4775.
- 31 Y. Li, K. Sheng, W. Yuan and G. Shi, *Chem. Commun.*, 2013, **49**, 291–293.
- 32 J. Sun, Y. Huang, C. Fu, Y. Huang, M. Zhu, X. Tao, C. Zhi and H. Hu, *J. Mater. Chem. A*, 2016, **4**, 14877–14883.
- 33 Z. Yu, J. Moore, J. Calderon, L. Zhai and J. Thomas, *Small*, 2015, **11**, 5289–5295.
- 34 Z. Zhang, F. Xiao and S. Wang, *J. Mater. Chem. A*, 2015, **3**, 11215–11223.
- 35 A. Ramadoss, K.-N. Kang, H.-J. Ahn, S.-I. Kim, S.-T. Ryu and J.-H. Jang, *J. Mater. Chem. A*, 2016, **4**, 4718–4727.
- 36 X. Pu, L. Li, M. Liu, C. Jiang, C. Du, Z. Zhao, W. Hu and Z. L. Wang, *Adv. Mater.*, 2016, **28**, 98–105.
- 37 G. Decher, *Science*, 1997, **277**, 1232–1237.
- 38 F. Caruso, R. A. Caruso and H. Möhwald, *Science*, 1998, **282**, 1111–1114.
- 39 S. W. Lee, N. Yabuuchi, B. M. Gallant, S. Chen, B.-S. Kim, P. T. Hammond and Y. Shao-Horn, *Nat. Nanotechnol.*, 2010, **5**, 531–537.
- 40 Y. Kim, J. Zhu, B. Yeom, M. D. Prima, X. Su, J.-G. Kim, S. J. Yoo, C. Uher and N. A. Kotov, *Nature*, 2013, **500**, 59–63.
- 41 S. Lyu, Y. Chen, S. Han, L. Guo, Z. Chen, Y. Lu, Y. Chen, N. Yang and S. Wang, *RSC Adv.*, 2018, **8**, 13191–13199.
- 42 M. Park, Y. Kim, Y. Ko, S. Cheong, S. W. Ryu and J. Cho, *J. Am. Chem. Soc.*, 2014, **136**, 17213–17223.
- 43 S. Cheong, J.-K. Kim and J. Cho, *Nanoscale*, 2016, **8**, 18315–18325.
- 44 Y. Kim and J. Cho, *Macromol. Res.*, 2009, **17**, 5–7.
- 45 M. Yoon, J. Choi and J. Cho, *Chem. Mater.*, 2013, **25**, 1735–1743.
- 46 D. Kim, S. Cheong, Y. G. Ahn, S. W. Ryu, J.-K. Kim and J. Cho, *Nanoscale*, 2016, **8**, 7000–7016.
- 47 I. Cho, H. Jung, B. G. Jeong, J. H. Chang, Y. Kim, K. Char, D. C. Lee, C. Lee, J. Cho and W. K. Bae, *ACS Nano*, 2017, **11**, 684–692.
- 48 Y. Ko, D. Shin, B. Koo, S. W. Lee, W.-S. Yoon and J. Cho, *Nano Energy*, 2015, **12**, 612–625.
- 49 D. Shin, Y. Ko and J. Cho, *RSC Adv.*, 2016, **6**, 21844–21853.
- 50 M. Park, Y. Kim, Y. Ko, S. Cheong, S. W. Ryu and J. Cho, *J. Am. Chem. Soc.*, 2014, **136**, 17213–17223.
- 51 M. Brust, M. Walker, D. Bethell, D. J. Schiffrin and R. Whyman, *J. Chem. Soc., Chem. Commun.*, 1994, **0**, 801–802.
- 52 S. Sun, H. Zeng, D. B. Robinson, S. Raoux, P. M. Rice, S. X. Wang and G. Li, *J. Am. Chem. Soc.*, 2004, **126**, 273–279.
- 53 J. Park, K. An, Y. Hwang, J.-G. Park, H.-J. Noh, J.-Y. Kim, J.-H. Park, N.-M. Hwang and T. Hyeon, *Nat. Mater.*, 2004, **3**, 891–895.
- 54 D. Buttry, *Advances in Electroanalytical Chemistry: Applications of the QCM to Electrochemistry*, Marcel Dekker, New York, 1991.
- 55 S. Zhang and N. Pan, *Adv. Energy Mater.*, 2015, **5**, 1401401.
- 56 N.-L. Wu, S.-Y. Wang, C.-Y. Han, D.-S. Wu and L.-R. Shiue, *J. Power Sources*, 2003, **113**, 173–178.
- 57 N. Jabeen, A. Hussain, Q. Xia, S. Sun, J. Zhu and H. Xia, *Adv. Mater.*, 2017, **29**, 1700804.
- 58 S. Phadke, S. Amara and M. Anouti, *ChemPhysChem*, 2017, **18**, 2364–2373.
- 59 M. D. Stoller and R. S. Ruoff, *Energy Environ. Sci.*, 2010, **3**, 1294–1301.
- 60 N. Liu, W. Ma, J. Tao, X. Zhang, J. Su, L. Li, C. Yang, Y. Gao, D. Golberg and Y. Bando, *Adv. Mater.*, 2013, **25**, 4925–4931.
- 61 Y. Li, X. Yan, X. Zheng, H. Si, M. Li, Y. Liu, Y. Sun, Y. Jiang and Y. Zhang, *J. Mater. Chem. A*, 2016, **4**, 17704–17710.
- 62 H. Xu, X. Hu, Y. Sun, H. Yang, X. Liu and Y. Huang, *Nano Res.*, 2015, **8**, 1148–1158.
- 63 J. Yu, W. Lu, J. P. Smith, K. S. Booksh, L. Meng, Y. Huang, Q. Li, J.-H. Byun, Y. Oh, Y. Yan and T.-W. Chou, *Adv. Energy Mater.*, 2017, **7**, 1600976.